Simulation and analysis of the current–voltage–temperature characteristics of Al/Ti/4H-SiC Schottky barrier diodes

Kamal Zeghdar[1], Lakhdar Dehimi[1,2], Fortunato Pezzimenti[3*], Sandro Rao[3], and Francesco G. Della Corte[3]

[1]*Laboratory of Metallic and Semi-conducting Materials (LMSM), University of Biskra, BP 145, 07000 Biskra, Algeria.*
[2]*Faculty of Material Science, University of Batna, 05000 Batna, Algeria.*
[3]*DIIES –Mediterranea University of Reggio Calabria, 89122 Reggio Calabria, Italy.*

*E-mail: fortunato.pezzimenti@unirc.it

Abstract - The current-voltage characteristics of Al/Ti/4H-SiC Schottky barrier diodes (SBDs) have been investigated in the 85-445 K temperature range by means of a combined numerical and analytical simulation study. Simulation results showed a good agreement with measurements in the whole explored current range from 10 μA to 10 mA. The main device electrical parameters, namely the barrier height and ideality factor, were found to be strongly temperature-dependent. In particular, the ideality factor decreases while the barrier height increases with increasing temperature. The observed behaviours have been successfully interpreted by using the thermionic emission (TE) theory with a triple Gaussian distribution of the barrier height (BH) in three different temperature ranges, i.e. $85 \leq \Delta T_1 \leq 135$ K, $180 \leq \Delta T_2 \leq 270$ K, and $315 \leq \Delta T_3 \leq 445$ K. The corresponding Richardson constants are $A_1^* = 149.26$ A·cm^{-2}K^{-2}, $A_2^* = 138.19$ A·cm^{-2}K^{-2}, and $A_3^* = 173.21$ A·cm^{-2}K^{-2}, respectively. These values are close to the theoretical result of 146 A·cm^{-2}K^{-2} expected for n-type 4H-SiC. Finally, it has been highlighted that the current flowing through the Schottky junction is also determined by the thermionic field emission (TFE) mechanism.

Japanese Journal of Applied Physics, n. 58, pp. 14002, 2019.
https://doi.org/10.7567/1347-4065/aaf3ab

1. Introduction

Silicon carbide (SiC) has recently gained a great attention as a wide band-gap semiconductor to be used in high-frequency high-power applications requiring high-temperature operation and/or high radiation-damage resistance.[1-5] The excellent electronic properties in terms of breakdown electric field strength, thermal conductivity, and relatively high electron mobility make SiC attractive for fabrication of power devices with die-sizes and reduced power losses.[6]

In this context, SiC-based Schottky contacts have been extensively proposed for understanding the material physics and to lead the design of new devices for harsh-environments.[7,8] In particular, during the last decade, many publications treated about the use of the aluminium/titanium (Al/Ti) alloy for fabrication of high-performance Schottky diodes.[9-12]

The current-voltage (*I-V*) characteristics of Schottky barrier diodes (SBDs) measured at room temperature do not provide detailed information about the nature of the barrier and the charge transport processes at the metal-semiconductor (MS) interface. On the contrary, the temperature dependent *I-V* behaviours are useful for giving a better understanding of the conduction mechanisms through the MS interface.[13,14] The fundamental mechanisms of carrier transport through the barrier might be, in principle, thermionic emission (TE), thermionic-field emission (TFE), recombination-generation (RG), and tunneling phenomena through the barrier.[15]

Titanium (Ti) is traditionally used as Schottky contact because it has a low Schottky barrier height (SBH) which results in a low forward voltage drop. However, Ti/SiC SBDs often show undesirable *I-V* characteristics that reveal abnormal variations of both the barrier height (BH) and ideality factor with temperature.[16,17] Several explanations for the origin of such anomalies have been proposed for a large variety of structures by taking into account the interface state density distribution,[18] the recombination and quantum-mechanical tunneling,[19,20] the image-force lowering,[21] and the lateral distribution of BH inhomogeneities [22,23] as well as the unusual high level of TFE dominating the device current capabilities.[24] In order to attain a complete understanding of the Schottky diode characteristics it is therefore necessary to model the *I-V-T* curves by using detailed physical models starting from specific assumptions.[25,26]

In this paper, the experimental forward *I-V* characteristics of Al/Ti/4H-SiC SBDs are investigated by means of a combined numerical and analytical simulation study which involves different current transport mechanisms in a wide range of temperatures (85-445 K). More in detail, by decreasing the temperature, an increase of the diode ideality factor, a decrease of the

apparent barrier height, and significant deviations from linearity of the Richardson plot are shown. The temperature dependencies of the current transport parameters have been successfully explained on the basis of the TE mechanism by assuming the coexistence of a triple Gaussian distribution of the barrier height around the MS interface in three different temperature ranges. Finally, the current through the junction appeared also influenced by the TFE theory that allows to properly fit the experimental ideality factor behaviour especially at low temperatures.

2. Device structure

A schematic cross sectional view of the 4H-SiC Schottky diodes considered in this work is shown in Fig. 1 (plot not in scale).

The experimental devices were fabricated and provided by the CNR-Institute for Microelectronics and Microsystems (IMM), unit of Bologna (Italy). They are based on a commercial available <0001> 7°62' off-axis n/n^+4H-SiC epitaxial wafer with a resistivity of 0.021 Ω×cm. The epi-layer is 16.5 μm-thick and has a net doping density of 3×10^{15} cm^{-3}. The fabrication process involves standard technological steps ensuring good reproducibility of the samples. A sequence of Ti (80 nm) and Al (350 nm) was deposited by sputtering and then photolithography and wet chemical etching were used to define Schottky square contacts with an active area of 2.25×10^4 μm^2. Finally, a 150 nm-thick nickel (Ni) film was deposited on the n^+ back surface of the wafer to form the cathode contact and an annealing treatment was performed in vacuum at 1000 °C for 2 min. Further details about the diode fabrication process are provided in Refs. 17, 27, and reference therein.

3. Physical models and parameters

The numerical simulation analysis of the diode current-voltage-temperature (*I-V-T*) characteristics was carried out by using the Atals-Silvaco 2D physical simulator [28] solving the Poisson's equation and the carrier continuity equations for a finely meshed device structure.

In order to fit the experimental curves, we carefully taken into account fundamental physical models such as the Shockley–Read–Hall (SRH) and Auger recombination processes, the band-gap temperature dependence and apparent band-gap narrowing (BGN), the concentration and temperature-dependent carrier mobility, the incomplete ionization of dopants, and the Schottky thermionic emission model involving the field-dependent barrier

lowering effect.

The temperature dependence of the 4H-SiC band-gap is assumed in the form of [29)]

$$E_g(T) = E_{g0} - \alpha(T - 300) \tag{1}$$

where $\alpha = 3.3 \times 10^{-4}$ eV/K is a specific material parameter, and $E_{g0} = 3.26$ eV is the band-gap energy at $T = 300$ K.

An apparent band-gap narrowing effect as a function of the activated doping in the n-type and p-type regions, i.e. ΔE_{gn} and ΔE_{gp}, respectively, is accounted for according to the Lindefelt's model of the band edge displacements:[30)]

$$\Delta E_{gn,p} = A_{n,p}\left(\frac{N_{D,A}^{+\,-}}{10^{18}}\right)^{1/2} + B_{n,p}\left(\frac{N_{D,A}^{+\,-}}{10^{18}}\right)^{1/3} + C_{n,p}\left(\frac{N_{D,A}^{+\,-}}{10^{18}}\right)^{1/4} \tag{2}$$

where $A_{n,p}$, $B_{n,p}$ and $C_{n,p}$, are appropriate 4H-SiC constants listed in Table I.[31)]

For the doping- and temperature-dependent low-field carrier mobility, the Caughey and Thomas mobility model is used: [32)]

$$\mu_{n,p} = \mu_{0n.p}^{min}\left(\frac{T}{300}\right)^{\alpha_{np}} + \frac{\mu_{0n.p}^{max}\left(\frac{T}{300}\right)^{\beta_{n.p}} - \mu_{0n\,p}^{min}\left(\frac{T}{300}\right)^{\alpha_{n.p}}}{1+\left(\frac{T}{300}\right)^{\gamma_{n.p}}\left(\frac{N}{N_{n.p}^{crit}}\right)^{\delta_{n.p}}} \tag{3}$$

where N is the local concentration of the ionized impurities and the parameters μ_0^{min}, μ_0^{max}, N^{crit}, α, β, γ, and δ are taken from Refs. 29 and 32 and summarized in Table II.

Assuming the Fermi-Dirac statistics, the incomplete ionization of impurities can be expressed by means of [31,33)]

$$N_{A,D}^{-+} = N_{A,D}\left(\frac{-1+\sqrt{1+4g_{V,C}\frac{N_{A,D}}{N_{V,C}^{(T)}}e^{\frac{\Delta E_{A,D}}{kT}}}}{2g_{V,C}\frac{N_{A,D}}{N_{V,C}^{(T)}}e^{\frac{\Delta E_{A,D}}{kT}}}\right) \tag{4}$$

where N_D and N_A are the n-type and p-type doping concentrations, ΔE_D and ΔE_A are the donor and acceptor energy levels, and $g_C = 2$ and $g_V = 4$ are the appropriate degeneracy factors of the conduction and valence band, respectively. N_C and N_V are the electron and hole density of states varying with temperature as given by [31)]

$$N_{C,V}(T) = N_{C,V\ 300}\left(\frac{T}{300}\right)^{3/2}. \tag{5}$$

Here, $N_{C\,300} = 1.66\times10^{19}$ cm^{-3} and $N_{V\,300} = 3.29\times10^{19}$ cm^{-3} are the electron and hole density of states at room temperature.

The Auger and SRH recombination rates are modelled using the standard expressions [34)]

$$R_{Auger} = \left(C_n n + C_p p\right)(np - n_i^2) \tag{6}$$

$$R_{SRH} = \frac{np - n_i^2}{\tau_n\left(p + n_i exp\left(-\frac{E_{trap}}{kT}\right)\right) + \tau_p\left(n + n_i exp\left(\frac{E_{trap}}{kT}\right)\right)} \tag{7}$$

where $C_n = 5\times10^{-31}$ cm^{6}s^{-1} and $C_p = 2\times10^{-31}$ cm^{6}s^{-1} are the Auger coefficients,[35)] E_{trap} is the difference between the trap energy level and the intrinsic Fermi level, and τ_n and τ_p are the carrier lifetimes modeled through the semi-empirical formula proposed in Ref. 36 considering a temperature dependence described by a power law [29)]

$$\tau_{n,p} = \frac{\tau_{0n,p}\left(\frac{T}{300}\right)^{\theta n,p}}{1+\left(\frac{N}{N_{n,p}^{SRH}}\right)} \ . \tag{8}$$

Here, N is the local doping concentration, $\tau_{0n} = 500$ ns and $\tau_{0p} = 100$ ns are process-dependent parameters, and $N_{n,p}^{SRH} = 5 \times 10^{16}$ cm^{-3} is a reference constant.[37)]

Finally, the barrier height $\emptyset_B$ is modelled with the standard expression [15)]

$$\emptyset_B = (\theta_M - \chi_s) \tag{9}$$

where the metal work function θ_M was fixed to 4.33 eV,[38)] and the electron affinity χ_s was used as fitting parameter as in Ref. 39.

It must be noted that the assumed simulation setup has also been used in other recent manuscripts of ours,[40-44)] and it is supported by experimental results on both Schottky and p-i-n diodes.[9,45-47)]

4. Results and discussion

4.1 *I-V-T* characteristics

The measured and simulated forward *I-V-T* curves of the considered Al/Ti/4H-SiC SBDs for ten different temperatures from 85 K to 445 K are shown in Fig. 2. For the measurements, an Agilent HP4155B semiconductor parameter analyser was used. The diodes were current biased in the range 10 μA ≤ *I* ≤ 10 mA with a current resolution of 10 nA.

It is worth noting that the numerical simulation results are in good agreement with the experimental data. During the simulations, a shunt resistance in the order of $1.3\times10^5\ \Omega$ was added to account for the diode low-voltage resistance effects due to the side-wall leakage and other leakage paths in the device structure.

By assuming the TE theory in the current range where the series resistance effect is negligible for each temperature, the current-voltage conduction model can be considered in the form of [48)]

$$I = I_0\, exp^{\left(\frac{qV}{nkT}\right)}\left[1 - exp^{\left(-\frac{qV}{kT}\right)}\right] \tag{10}$$

where n is the ideality factor, V is the diode bias voltage, q is the electronic charge, k is the Boltzmann constant, and I_0 is the saturation current given by:

$$I_0 = AA^*T^2e^{\left(-\frac{q\emptyset_B}{kT}\right)} \tag{11}$$

where $\emptyset_B$ is the barrier height, A is the area of the diode, and A^* is the Richardson constant that takes into account the quantum mechanical reflections and tunneling phenomena. Its value is theoretically in the order of 146 $Acm^{-2}K^{-2}$ for n-type 4H-SiC.[49)]

From the experimental *I-V-T* curves in Fig. 2 we extracted the fundamental diode parameters I_0, $\emptyset_B$, and n similarly to Ref. 50. In particular, at each temperature, the saturation current I_0 was determined from the intercept of the plot $ln(I)$ vs. V for $V = 0$. Afterwards, the barrier height $\emptyset_B$ was calculated from Eq. (11) resulting $\emptyset_B = (kT/q)ln(AA^*T^2/I_0)$. Finally, the ideality factor n was extracted determining the slope of the linear region of the curves $ln(I)$ vs. V for $50 \leq I \leq 500$ μA.

The n and $\emptyset_B$ behaviours as a function of temperature are shown in Fig. 3. As can be seen, the ideality factor decreases while the barrier height increases with increasing temperature.

By considering Eq. (11) in the form of $ln(I_0/T^2) = ln(AA^*) - (q/kT)\emptyset_B$, the Arrhenius plot of term $ln(I_0/T^2)$ against $1000/T$ is shown in Fig. 4.

The Arrhenius plot shows a significant deviation of the term $ln(I_0/T^2)$ from linearity at low temperatures and the data fit asymptotically to a straight line only at higher temperatures ($T > 270$ K). From the slope of this straight line, an activation energy of 0.82 eV was obtained. At the same time, from the line intercept with the ordinate axis, the Richardson constant A^* results 4.64×10^{-4} $A\cdot cm^{-2}K^{-2}$, namely a much lower value than the theoretical one expected for n-type 4H-SiC.

The presented results seem to predict current transport mechanisms not following the pure TE theory and the existence of barrier inhomogeneities need to be evaluated.

4.2 The image force effect

In order to understand the factors influencing the BH lowering and the ideality factor increase with decreasing temperature, the image-force effect was considered at first. In particular, the BH lowering due to the image-force mechanism was modelled in the form of [51)]

$$\Delta\emptyset = \left\{\left(\frac{q^3 N}{8\pi^2 \varepsilon_s^3}\right)\left[\emptyset_B - V - \zeta - \frac{kT}{q}\right]\right\}^{1/4} \tag{12}$$

where V is the applied bias voltage, $\mathcal{E}_s = 9.6\mathcal{E}_0$ is the material permittivity, N is the ionized impurity concentration, and $\zeta = kT\ln(N_C/N_D)$.

The calculated $\Delta\emptyset$ varies from 8.816 meV to 16.983 meV in the 85-443 K temperature range for the barrier height $\emptyset_B$ ranging from 0.421 eV to 1.305 eV as in Fig. 3. These results point out that the influence of the barrier lowering due to the image-force on $\emptyset_B$ is nearly constant and the image-force effect alone cannot determine the observed device characteristics. At the same time, the diode ideality factor can be calculated by using the following expression [51)]

$$\frac{1}{n} = 1 - \frac{1}{4}\left(\frac{q^3 N}{8\pi^2 \varepsilon_s^3}\right)^{\frac{1}{4}}\left[\emptyset_B - V - \zeta - \frac{kT}{q}\right]^{-\frac{3}{4}} \tag{13}$$

It varies from 1.006 to 1.014 showing a negligible effect of the image-force lowering on the device forward current behaviour. In addition, the n value is very close to 1 predicting an almost unrealistic homogenous barrier at the diode interface.

4.3 Inhomogeneous barrier analysis

In this section, the $\emptyset_B$ and n anomalous behaviours reported above are explained by assuming spatially inhomogeneous barrier heights and potential fluctuations at the Schottky interface that consist of low and high barrier areas as suggested by Werner and Guttler in Ref. 23. More in detail, the spatial barrier inhomogeneities in SBDs are described by assuming a Gaussian distribution $\rho(\emptyset_B)$ of the SBH with a standard deviation σ around a mean value $\overline{\emptyset_B}$:

$$\rho(\emptyset_B) = \frac{1}{\sigma\sqrt{2\pi}} e^{-\frac{\left(\emptyset_B - \overline{\emptyset_B}\right)^2}{2\sigma^2}} \quad . \tag{14}$$

The pre-exponential term is a normalization constant. The total forward current across the Schottky barrier diode is given by:

$$I = \int i(V, \emptyset_B)\rho(\emptyset_B)d\emptyset_B \tag{15}$$

where $i(\mathrm{V}, \emptyset_{\mathrm{B}})$ is the current based on the TE model in Eq. (10). It is assumed that $\overline{\emptyset}_{\mathrm{B}}$ and σ are linearly bias-dependent on Gaussian parameters as follows:

$$\overline{\emptyset_{\mathrm{B}}} = \overline{\emptyset}_{B0} + \rho_2 \mathrm{V} \tag{16}$$

$$\sigma^2 = {\sigma_0}^2 + \rho_3 \mathrm{V} \tag{17}$$

where $\overline{\emptyset}_{B0}$ and σ_0 are the zero-bias reference parameters, and ρ_2 and ρ_3 are temperature-independent voltage coefficients which model the voltage deformation of the barrier distribution.

By introducing $i(\mathrm{V}, \emptyset_{\mathrm{B}})$ and $\rho(\emptyset_B)$ from Eqs. (10) and (14) into Eq. (15), and performing the integration we can write:

$$I = AA^*T^2\left[-\frac{q}{kT}\left(\overline{\emptyset}_{B0} - \frac{q\sigma_0^2}{2kT}\right)\right] exp\left(\frac{qV}{n_{ap}kT}\right)\left[1 - exp\left(-\frac{qV}{kT}\right)\right] \tag{18}$$

$$I_0 = AA^*T^2 exp\left(-\frac{q\emptyset_{Bap}}{kT}\right) \tag{19}$$

where $\emptyset_{B\mathrm{ap}}$ and n_{ap} are the apparent SBH and ideality factor in the form of

$$\emptyset_{Bap} = \overline{\emptyset}_{B0} - \frac{q\sigma_0^2}{2kT} \tag{20}$$

$$\frac{1}{n_{ap}} - 1 = -\rho_2 + \frac{q\rho_3}{2kT} \ . \tag{21}$$

The plot of the apparent barrier height and ideality factor as a function of $q/2kT$ aids to characterize the behaviour of the inhomogeneous potential barrier as shown in Fig. 5 and Fig. 6, respectively.

From Fig. 5, $\overline{\emptyset}_{B0}$ is the intercept and σ_0 is the slope of the straight line of the best linear fit calculated considering three different temperature ranges, namely 85 ≤ ΔT_1 ≤ 135 K, 180 ≤ ΔT_2 ≤ 270 K, and 315 ≤ ΔT_3 ≤ 445 K. In particular, the $\overline{\emptyset}_{B0}$ and σ_0 values are 1.05 eV and 0.096 in the range ΔT_1, 1.543 eV and 0.15 in the range ΔT_2, and 1.643 eV and 0.169 in the range ΔT_3, respectively.

Similarly, from the plot of the term $(n_{ap}^{-1} - 1)$ vs. $q/2kT$ in Fig. 6, we calculated the coefficients ρ_2 as the intercept and ρ_3 as the slope of the straight line which fits the diode data for each temperature range. It results, ρ_2 = 0.403 V and ρ_3 = -0.005 V in the range ΔT_1, ρ_2 = 0.141 V and ρ_3 = -0.012 V in the range ΔT_2, and ρ_2 = 0.276 V and ρ_3 = -0.004 V in the range ΔT_3, respectively.

This analysis, predicting three different Gaussian distributions of the barrier height at the Ti/4H–SiC interface, suggests that the current transport is controlled in turn by different mechanisms at different temperature ranges. More in detail, the temperature dependence of the density of states in the n-type 4H-SiC conduction band (see Eq. (5)) contributes to the reduction of the energy difference between the conduction band minimum E_C and the Fermi level E_F expressed by

$$(E_C - E_F) = kTln\,(N_C/N_D)\,. \tag{22}$$

Although, the ideal barrier height $\emptyset_B$ in Eq. (9) is not affected by this difference, an effective reduction of the term $(E_C - E_F)$ tends to increase the tunneling effects through the barrier determining de facto different behaviours of the apparent barrier height $\emptyset_{Bap}$ with temperature.

Finally, by combining Eqs. (19) and (20), we obtain:

$$ln\left(\frac{I_0}{T^2}\right) - \left(\frac{q^2\sigma_0^2}{2k^2T^2}\right) = ln(AA^*) - \left(\frac{q\overline{\emptyset_{B0}}}{kT}\right). \tag{23}$$

The slope and the intercept of the linear fitting of the plot $ln(I_0/T^2) - (q^2\sigma_0^2/2k^2T^2)$ vs. q/kT (see Fig. 7) allow to determine $\overline{\emptyset}_{B0}$ and A^* as follows: 1.05 eV and 149.26 A·cm^{-2}K^{-2} in the range ΔT_1, 1.543 eV and 138.19 A·cm^{-2}K^{-2} in the range ΔT_2, and 1.649 eV and 173.21 A·cm^{-2}K^{-2} V in the range ΔT_3, respectively.

It is worthwhile noting that $\overline{\emptyset}_{B0}$ is in good agreement with the results in Fig. 5. At the same time, the modified Richardson constants are close around the expected theoretical value.

4.4 Thermionic field emission transport

If the current transport is controlled by the thermionic field emission theory, the relationship between the diode current and voltage can be expressed by using [51)]

$$I = I_0\, exp^{\left(\frac{qV}{E_0}\right)} \tag{24}$$

where the term E_0 is related to the tunnel phenomena that increase for increasing temperatures and it is defined by means of the characteristic tunneling energy E_{00} as follows:

$$E_0 = E_{00}\coth\left(\frac{E_{00}}{kT}\right) \tag{25}$$

$$E_{00} = \frac{qh}{4\pi}\left(\frac{N_D}{m^*\varepsilon_s}\right)^{1/2} . \tag{26}$$

Here, h is the Planck constant and $m^*= 0.2\ m_0$ is the effective electron mass.[52)]

Depending on the diode temperature, if E_0 tends to kT, i.e. $kT >> E_{00}$, the current transport corresponds to the ideal thermionic emission. On the other hand, for temperatures such those $kT \sim E_{00}$ the thermionic field emission should be considered and the ideality factor of the *I-V* curves is calculated from Eqs. (24) and (25) as $n = E_0/kT$.

By considering the current mechanisms through the junction dominated by the TFE effect, the ideality factor behaviour as a function of the temperature for different values of E_{00} is shown in Fig. 8. Here, the n values extracted from the experimental *I-V* curves in Fig. 2 are also reported for comparison.

It is observed that the experimental dependence of n from temperature is in good agreement with the theoretical curve for $E_{00} = 31.5$ meV up to T is in the limit of about 230 K. This value of E_{00} corresponds in Eq. (26) to a theoretical donor concentration in the order of 6×10^{18} cm^{-3}.

In accordance with the analysis developed in Ref. 53, we can assume that the energy E_{00} determines the real BH profile. From Eq. (26), its value is mainly related to the effective carrier concentration and dielectric constant as well as to the density of states through the electron mass. In other words, depending on the diode operation conditions (i.e., bias voltage and temperature) a local enhancement of the electric field can determine a local reduction of the barrier height and therefore an enhanced tunneling probability.

5. Conclusion

In this work, we have simulated the *I-V-T* characteristics of Al/Ti/4H-SiC Schottky barrier diodes to study the effect of temperature on the main device electrical parameters. By fitting the experimental results in the 85-443 K temperature range, we found an increase of the barrier height and a decrease of the ideality factor with increasing temperature. The origin of these behaviours has been explained on the basis of the thermionic emission mechanism with a triple Gaussian distribution of the barrier heights around the Ti/4H–SiC interface in three different

temperature ranges. The corresponding Richardson constants were in good agreement with the expected theoretical value of 146 $A \cdot cm^{-2}K^{-2}$ for *n*-type 4H-SiC.

Different current transport mechanisms have been investigated. In particular, the effect of the image force on the *I-V-T* curves cannot alone determine the observed device characteristics, predicting an almost unrealistic homogenous barrier at the diode MS interface. On the contrary, the current through the junction appeared influenced by the thermionic field emission theory that allows to properly fit the ideality factor behaviour up to temperatures in the limit of 230 K.

References

1) M. C. Lee, and A. Q. Huang, Solid-State Electron. **93**, 27-39 (2014).
2) M. L. Megherbi, F. Pezzimenti, L. Dehimi, M. A. Saadoune, and F. G. Della Corte, IEEE Trans. Electron Dev. **65**, 3371-3378 (2018).
3) R. Wang, D. Boroyevich, P. Ning, Z. Wang, F. Wang, P. Mattavelli, K. Ngo, and K. Rajashekara, IEEE Trans. Power Electron. **28**, 555-572 (2013).
4) G. De Martino, F. Pezzimenti, F. G. Della Corte, G. Adinolfi, and G. Graditi, IEEE Conf. on Ph.D. Research in Microelectronics and Electronics - PRIME, 2017, p. 221.
5) L. Lin, and J. H. Zhao, Solid-State Electron. **86**, 36-40 (2013).
6) B. J. Baliga, *Silicon carbide power devices* (World Scientific Publishing Co., 2005).
7) T. Nakamura, T. Miyanagi, I. Kamata, T. Jikimoto, and H. Tsuchida, IEEE Electron. Dev. Lett. **26**, 99- 101m (2005).
8) K. Vassilevski, I. Nikitina, P. Bhatnagar, A. Horsfall, N. Wright, N. O'Neill, M. Uren, K. Hilton, A. Munday, A. Hydes, and C. M. Johnson, Mater. Sci. Forum, **527**, 931-934 (2006).
9) A .Vassilevski, I. Nikitina, A. Horsfall, N. G. Wright, A. G. O'Neill, K. P. Hilton, A. G. Munday, A. J. Hydes, M. J. Uren, and C. M. Johnson, Mater. Sci. Forum **556**, 873-876 (2007).
10) S. Rao, G. Pangallo, F. Pezzimenti, and F. G. Della Corte, IEEE Electr. Device L. **36**, 720-722 (2015).
11) W. Yue-Hu, Z. Yi-Men, Z.Yu-Ming, S. Qing-Wen, and J. Ren-Xu, Chinese Phys. B **20**, 087305 (2011).
12) D. Perrone, M. Naretto, S. Ferrero, L. Scaltrito, and C. F. Pirri, Mater. Sci. Forum **615**, 647-650 (2009).
13) S. Chand, and J. Kumar, Semicond. Sci. Technol. **10**, 1680-1688 (1995).
14) S. Karatas, S. Altindal, and M. Caskar, Phys. B **357**, 386-397 (2005).
15) S. M. Sze, *Physics of semiconductor devices* (John Wiley and Sons,1982), Chaps. 1, 5, 9.
16) S. Kyoung, E. S. Jung, and M. Y.Sung, Microelectron. Eng. **154**, 69-73 (2016).
17) S. Rao, L. Benedetto, G. Pangallo, A. Rubino, S. Bellone, and F. G Della Corte, IEEE Sensors J. **16**, 6537-6542 (2016).
18) R. T. Tung, Mat. Sci. Eng. R. **35**, 1-138 (2001). DOI: 10.1016/S0927-796X(01)00037-7
19) M. K. Hudait, P. Venkateswarlu, and S. B. Krupanidhi, Solid-State Electron. **45**, 133-141 (2001).
20) D. Donoval, M. Barus, and M. Zdimal, Solid-State Electron. **34**, 1365–1373 (1991).
21) M. Barus, and D. Donoval, Solid-State Electron. **36**, 969-974 (1993).
22) R. T. Tung, J. P. Sullivan, and F. Schrey, Mat. Sci. Eng. B **14**, 266-280 (1992).
23) J. H. Werner, and H. H. Guttler, J. Appl. Phys. **69**, 1522 (1991).
24) Z. J Horvath, A. Bosacchi, S. Franchi, E. Gombia, R. Mosca, and A. Motta, Mat. Sci. Eng. B **28**, 429-432 (1994).
25) P. Kaushal, S. Chand, and J. Osvald, Intl. J. Electron. **100**, 686-698 (2013).
26) P. Kaushal, and S. Chand, Intl. J. Electron. **103**, 937-949 (2015).
27) F. Moscatelli, A. Scorzoni, A. Poggi, G. C. Cardinali, and R. Nipoti, Mater. Sci. Forum, **457-460**, 993-996 (2004).
28) Silvaco-Atlas *User's Manual, Device Simulator Software* (2013).
29) X. Li, Y. Luo, L. Fursin, J. H. Zhao, M. Pan, P. Alexandrov, and M. Weiner, Solid-State Electron. **47**, 233-239 (2003).
30) U. Lindefelt, J. Appl. Phys. **84**, 2628-2637 (1998).
31) M. Ruff, H. Mitlehner, and R. Helbig, IEEE T. Electron. Dev. **41**, 1040-1054 (1994).
32) M. Roschke, and F. Schwierz, IEEE T. Electron. Dev. **48**, 1442-1447 (2001).

33) T. Troffer, M.Schadt, T. Frank, H.Itoh, G. Pensl, J. Heindl, and M. Maier, Phys. Status Solidi A **162**, 277-298 (1997).
34) S. Selberherr, *Analysis and Simulation of Semiconductor Devices* (Springer, 1984) Chap. 4.
35) A. Galeckas, J. Linnros, V. Grivickas, U. Lindefelt, and C. Hallin, Appl. Phys. Lett. **71**, 3269-3271 (1997).
36) P. T. Landsberg, and G. S. Kousik, J. Appl. Phys. **56**, 1696-1700 (1984).
37) M. Bakowski, U. Gustafsson and U. Lindefelt, Phys. Status Solidi A **162**, 421-429 (1997).
38) Z. C. Feng, and J. H. Zhao, *Silicon Carbide: Materials, Processing and Devices* (Taylor & Francis, 2004).
39) M. Philip, and A. O'Neill, IEEE Conf. on Optoelectronic and Microelectronic Materials and Devices, 2006, p. 137.
40) F. G. Della Corte, G. De Martino, F. Pezzimenti, G. Adinolfi, and G. Graditi, IEEE Trans. Electron Dev. **68**, 3352-3360 (2018).
41) F. Pezzimenti, IEEE T. Electron. Dev. **60**, 1404-1411 (2013).
42) F. Bouzid, F. Pezzimenti, L. Dehimi, M. L. Megherbi, and F. G. Della Corte, Jpn. J. Appl. Phys. **56**, 094301 (2017).
43) F. Pezzimenti, and F. G. Della Corte, Proc. Mediterranean Electrotechnical Conf. - MELECON, 2010, p. 1129.
44) Y. Marouf, L. Dehimi, F. Bouzid, F. Pezzimenti, and F. G. Della Corte, Optik **163**, 22-32 (2018).
45) M. L. Megherbi, F. Pezzimenti, L. Dehimi, A. Saadoune, and F. G. Della Corte, J. Electron. Mater. **47**, 1414-1420 (2018).
46) F. Bouzid, L. Dehimi, and F. Pezzimenti, J. Electron Mater. **46**, 6563-6570 (2017).
47) F. Pezzimenti, L. F. Albanese, S. Bellone, and F. G. Della Corte, IEEE Conf. on Bipolar/BiCMOS Circuits and Technology Meeting, BCTM 2009, p. 214.
48) E. H. Rhoderick, IEE Proc. I - Solid-State Electron. Dev. **129**, 1-14 (1982).
49) Z. Ouennoughi, S. Toumi, and R. Weiss, Phys. B. **456**, 176-181 (2015).
50) S. K. Cheung, and N. W. Cheung, Appl. Phys. Lett. **49,** 85 (1986).
51) E. H. Rhoderick, and R. H. Williams, *Metal-semiconductor contacts* (Clarendon Press, 1988) Chaps. 1, 3.
52) W. Gotz, A Schoner, G. Pensl, W. Suttrop, W. J. Choyke, R. Stein, and S. Leibenzeder, Mater. Sci. Forum, **117-118,** 495-500 (1993).
53) E. Ayyildiz, H. Cetin, and Z. J. Horvath, Appl. Surf. Sci. **252**, 1153-1158 (2005).

Figure Captions

Fig. 1. Al/Ti/4H-SiC Schottky barrier diode schematic cross section.

Fig. 2. Experimental (dotted lines) and simulated (solid lines) current–voltage characteristics of the Al/Ti/4H-SiC Schottky diode at different temperatures.

Fig. 3. Ideality factor and barrier height behaviours as a function of temperature for the device in Fig. 2.

Fig. 4. Arrhenius plot of $ln(I_0/T^2)$ vs. $1000/T$.

Fig. 5. $\emptyset_{Bap}$ vs. $q/2kT$ according to a Gaussian distribution of the SBH.

Fig. 6. $(n_{ap}^{-1} - 1)$ vs. $q/2kT$ according to a Gaussian distribution of the SBH.

Fig. 7. $ln(I_0/T^2) - (q^2\sigma_0^2/2k^2T^2)$ vs. q/kT according to a Gaussian distribution of the SBH.

Fig. 8. (Solid lines) Ideality factor as a function of the temperature for different values of E_{00}. (Dots) n values extracted from the experimental I-V curves in Fig. 2.

Table I. Apparent band-gap narrowing parameters.

	n	*p*
A	1.17×10^{-2}	1.54×10^{-3}
B	1.50×10^{-2}	1.30×10^{-2}
C	1.90×10^{-2}	1.57×10^{-2}

Table II. 4H-SiC carrier mobility parameters.

	n	*p*
μ_0^{min}(cm²/V·s)	40	15.9
μ_0^{max}(cm²/V·s)	950	125
N^{crit} (cm^{-3})	2×10^{17}	1.76×10^{19}
α	-0.50	-0.50
β	-2.40	-2.15
γ	-0.76	-0.34
δ	0.76	0.34

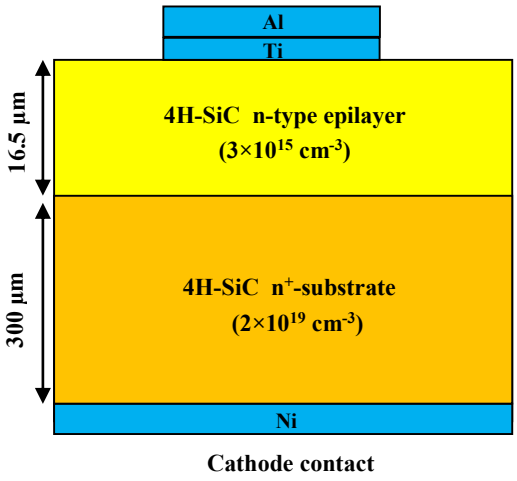
Al
Ti
16.5 µm
4H-SiC n-type epilayer
(3×10^15 cm^-3)
300 µm
4H-SiC n+-substrate
(2×10^19 cm^-3)
Ni
Cathode contact

Fig. 1

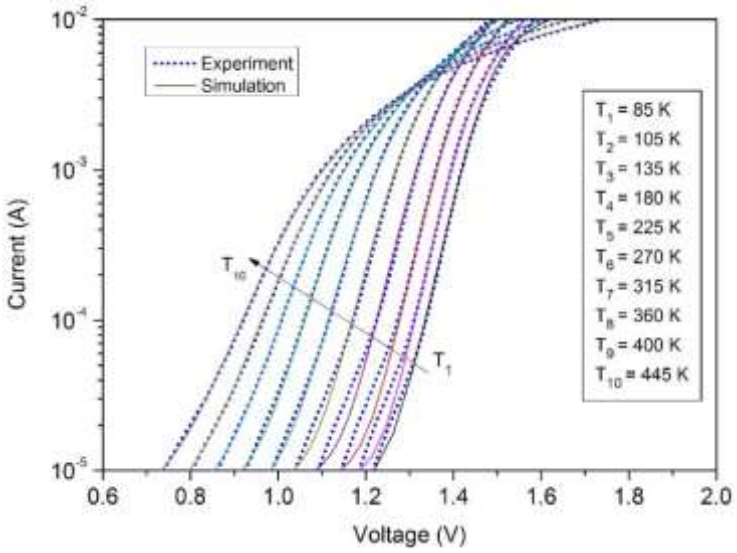
Experiment
Simulation
T_1 = 85 K
T_2 = 105 K
T_3 = 135 K
T_4 = 180 K
T_5 = 225 K
T_6 = 270 K
T_7 = 315 K
T_8 = 360 K
T_9 = 400 K
T_{10} = 445 K
T_{10}
T_1
Current (A)
Voltage (V)
10^{-2}
10^{-3}
10^{-4}
10^{-5}
0.6
0.8
1.0
1.2
1.4
1.6
1.8
2.0

Fig. 2

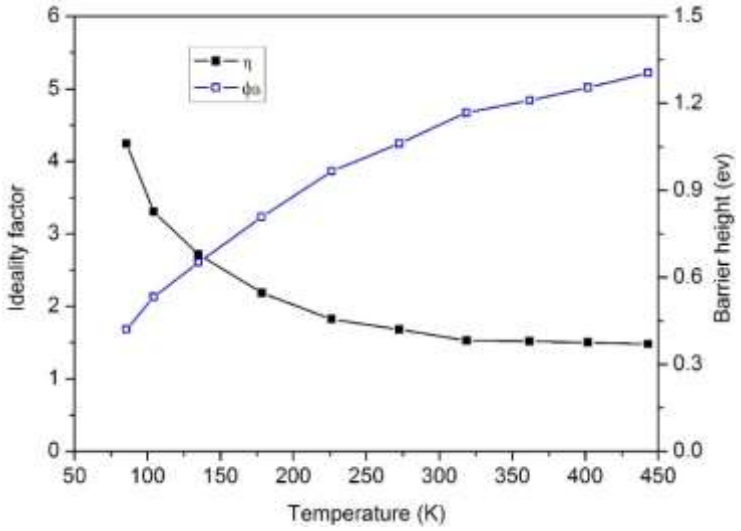
η
ϕb
Ideality factor
Barrier height (ev)
Temperature (K)
0
1
2
3
4
5
6
0.0
0.3
0.6
0.9
1.2
1.5
50
100
150
200
250
300
350
400
450

Fig. 3

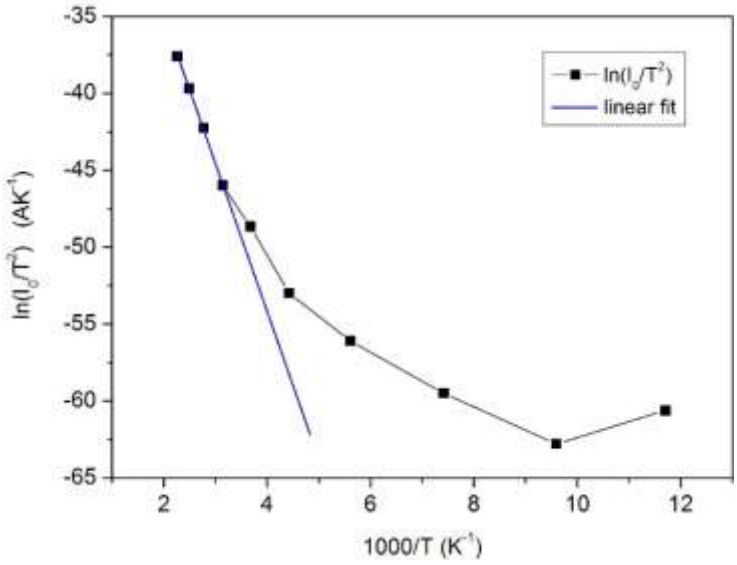
-35
-40
-45
-50
-55
-60
-65
2
4
6
8
10
12
ln(I0/T2) (AK-1)
1000/T (K-1)
ln(I0/T2)
linear fit

Fig. 4

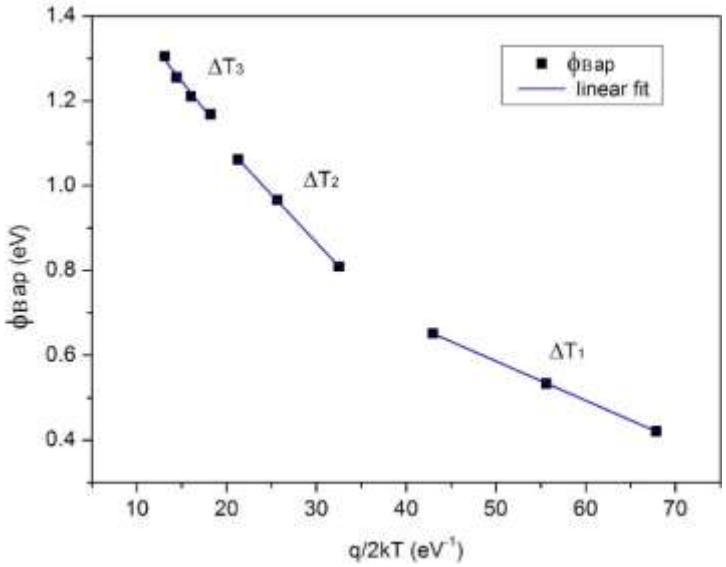
1.4
1.2
1.0
0.8
0.6
0.4
10
20
30
40
50
60
70
ΔT3
ΔT2
ΔT1
ϕBap
linear fit
ϕBap (eV)
q/2kT (eV-1)

Fig. 5

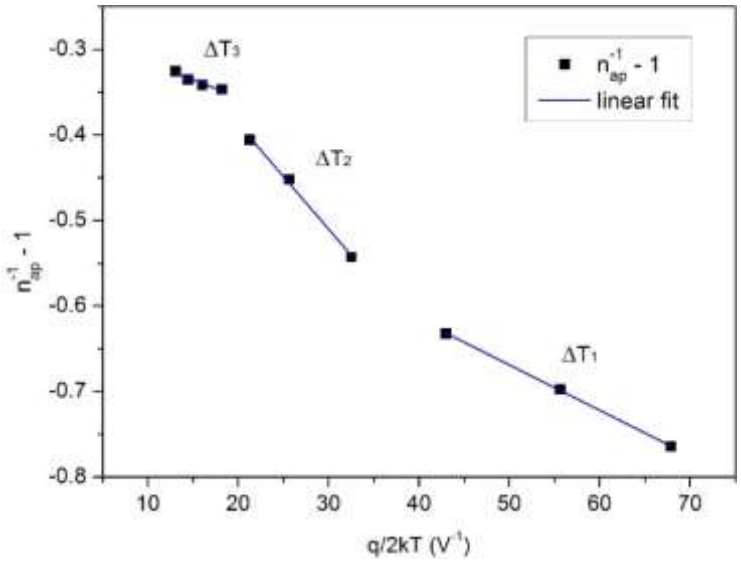
ΔT3
ΔT2
ΔT1
n-1ap - 1
linear fit
n-1ap - 1
q/2kT (V-1)
-0.3
-0.4
-0.5
-0.6
-0.7
-0.8
10
20
30
40
50
60
70

Fig. 6

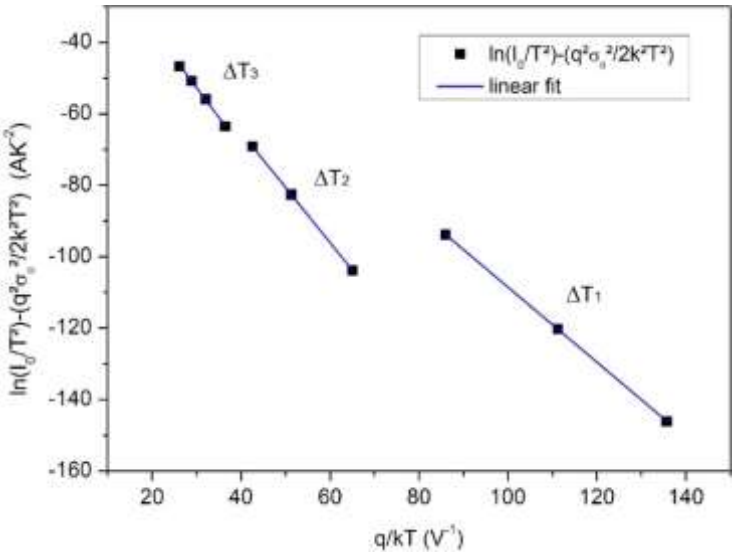
ln(I0/T4)-(q2σ02/2k2T2)
linear fit
ΔT3
ΔT2
ΔT1
-40
-60
-80
-100
-120
-140
-160
20
40
60
80
100
120
140
q/kT (V-1)

Fig. 7

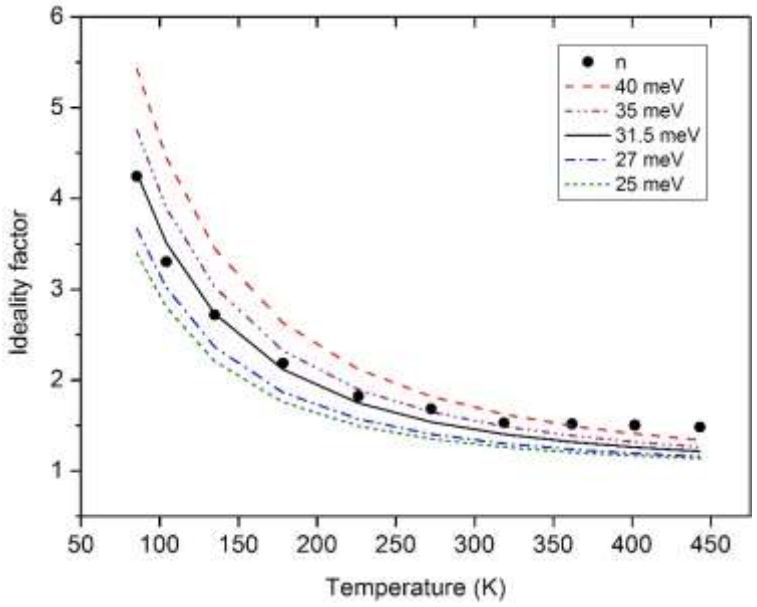
n
40 meV
35 meV
31.5 meV
27 meV
25 meV
Ideality factor
Temperature (K)
1
2
3
4
5
6
50
100
150
200
250
300
350
400
450

Fig. 8